Modeling the kinetics and microstructural evolution during static recrystallization

B. Radhakrishnan, G.B. Sarma and T. Zacharia

Modeling and Simulation Group, Oak Ridge National Laboratory
Oak Ridge, TN 37831-6140, USA

February 19, 1998

Abstract

The kinetics of microstructure and texture evolution during static recrystallization of a cold-rolled and annealed fcc material is simulated by coupling a finite element model of microstructural deformation with a Monte Carlo simulation of recrystallization. The salient features of the simulations include a nucleation model for recrystallization based on subgrain growth and the modeling of simultaneous recovery during recrystallization. The simulation results quantify the effects of non-uniform stored energy distribution and orientation gradients present in the cold-worked microstructure on recovery by subgrain growth, and hence on the spatial distribution of nuclei and their orientations. The growth of these recrystallized nuclei in the presence of continued recovery of the substructure has been simulated for initial cold work levels of $\varepsilon = 0.7$ and $\varepsilon = 1.1$ obtained by plane strain compression. The simulations are shown to be potentially capable of capturing the formation and evolution of cube texture commonly observed in cold-rolled and annealed fcc materials.

1 Introduction

In metals deformed under cold working conditions, part of the energy of deformation is stored as the increase in the dislocation density within the material [1]. The dislocation substructure that evolves during cold working is quite complex, and has been the subject of ongoing research for the past several decades [2–4]. Associated with the dislocation substructure is the formation of crystallographic texture, which is a consequence of the rotation of grains or parts of a grain in the microstructure. This rotation is necessary to accommodate an arbitrary deformation by crystallographic slip on a limited number of slip systems [5]. A further evolution of the microstructure that occurs during subsequent annealing of the cold-worked material is that associated with recovery and recrystallization processes. The local rearrangement of dislocations into lower energy configurations during recovery and the simultaneous or subsequent evolution of the substructure into a well defined high angle grain boundary network by recrystallization are again well documented in the literature for a wide variety of materials and processing conditions [6]. However, a quantitative understanding of the influence of the initial microstructure and deformation conditions on the subsequent evolution of microstructure and texture during annealing is still lacking. This is because the spatial variation of the dislocation substructure, which influences the evolution of the microstructure during recovery and recrystallization, is not known quantitatively.

An example of the inadequacy of simple analytical models to describe such a complex process as recrystallization is the classic analytical expression proposed by Johnson, Mehl, Avrami and Kolmogorov (JMAK) [6]. The recrystallized fraction, f_{rex}, is given by

$$f_{rex} = 1 - \exp(-rt^n), \tag{1}$$

where t is the time, r is a function of the nucleation rate, and the JMAK exponent n is

a function of both nucleation and growth rates. Equation (1) can be rewritten as

$$\ln[\ln(\frac{1}{1-f_{rex}})] = \ln(r) + n\ln(t). \tag{2}$$

Equation (2) yields a straight line of slope equal to the JMAK exponent n when the left hand side is plotted as a function of $\ln(t)$.

The JMAK analysis is based on the assumptions that the recrystallized nuclei form randomly in the cold-worked microstructure and that the growth of these nuclei is isotropic. The ideal JMAK behavior is rarely exhibited by real materials. For many materials, the JMAK exponent obtained experimentally is smaller than that predicted by the JMAK analysis. Also, the JMAK exponent varies during recrystallization, and a significantly smaller exponent is obtained at the later stages of recrystallization. Such a deviation from ideal JMAK behavior becomes more significant in the presence of recovery, non-uniform distribution of stored energy of deformation, non-random distribution of recrystallized nuclei, and anisotropic growth of the recrystallized nuclei. There have been several attempts to improve the JMAK model, one of which is the Microstructural Path Methodology (MPM) developed by Vandermeer and Rath [7]. MPM allows more detailed information about nucleation and growth rates to be extracted from experimental measurements than does the original JMAK analysis. However, the methodology is still based on the assumptions of random nuclei distribution and isotropic growth of recrystallization boundaries. Recently, Doherty *et al.* [8] have modified the JMAK analysis to include variable nucleation and growth rates during recrystallization. The JMAK exponent, n, has been represented as

$$n = 4 + m - 3g, \tag{3}$$

where m is related to the nucleation rate, N, as

$$N = N_0 t^m, \tag{4}$$

and g is related to the growth rate, G, as

$$G = G_0 t^{-g}, \tag{5}$$

where G_0 and N_0 are constants. The modified JMAK exponent is capable of taking into account the reduction in the recrystallization velocity due to simultaneous recovery and non-uniform distribution of stored energy of deformation. However, the analysis, as in the case of MPM, is still based on the assumptions of random distribution of nuclei and isotropic growth. It is important to note that none of the above analytical models can describe the orientations of the recrystallized nuclei, and hence, they are incapable of predicting the evolution of recrystallization textures.

In the last decade, several microstructural models have been developed for simulating the temporal evolution of recrystallization microstructures, as well as for predicting the recrystallization kinetics. These models can be grouped as cellular models [9–11], computer Avrami models [12–14], and models based on the Monte Carlo (MC) [15–18], and Cellular Automaton (CA) [19] techniques. The cellular models are based on the assumption that the smallest microstructural unit of importance during annealing is a grain or subgrain, with the microstructure being represented as a cellular structure by the position of the triple points. Boundary curvature is neglected under the assumption that the boundary mobility is high compared to the triple point mobility, so that the triple point motion is rate-controlling. The forces at a triple point are calculated, and based on the assumed mobility, the triple point velocity is calculated and the triple point moved to its new position. Such a model has been used to simulate the formation of a high angle boundary by the coarsening of subgrains in an orientation gradient [10].

In the Computer Avrami models, the spatial distribution of nuclei and variations in growth rate are handled by using a combination of analytical methods, and a binary tree construction is used in 2-d sections to locate the position of grain boundaries. The nuclei are initially placed in a 3-d box, and each nucleus is allowed to grow according to the local growth rate which is initially assigned arbitrarily to each of the nuclei. The model is very useful for a qualitative study of the effects of non-random nucleation and anisotropic growth on the recrystallization kinetics. However, there is no description of the cold-worked microstructure, and hence, there is no microstructural basis for the spatial distribution and growth rates of the nuclei.

The MC technique involves representing the continuum microstructure on a discrete set of regularly spaced grid of points (MC grid), associating a volume of material with each point, and evolving the microstructure according to some rules [15]. Each site is assigned a number which represents a crystallographic orientation, so that a grain is defined by a collection of grid points with the same number. Grain boundaries are not represented physically, but are assumed to exist between points with different orientation numbers. The nucleation process is not modeled explicitly. Rather, nuclei are added arbitrarily to the microstructure either in totality at the start of the simulation to capture site saturation effects, or continuously as a function of simulation time to model constant nucleation rate effects. The recrystallization model proceeds by randomly selecting grid points and changing the orientation number of the selected point to that of one of its nearest neighbors based on energy considerations. The energy of the point and its neighbors is computed before and after the change, with the change being allowed only if it leads to a reduction in energy. Such a reduction in energy occurs when the orientation of a cold-worked site is converted to that of a recrystallized neighbor, thus causing the movement of the boundaries between cold-worked and recrystallized regions.

In the above simulations [15], the stored energy of deformation was assumed to be uniform and the nuclei were placed randomly in the microstructure. The simulations

produced the theoretically expected values of the JMAK exponents for site-saturated and constant nucleation rate conditions. Subsequently, these simulations were extended to the case of heterogeneous nucleation by imposing certain conditions on the relative magnitudes of the stored energy of deformation and the grain boundary energy [16], and to the recrystallization of systems containing a fine dispersion of second-phase particles [17]. In the case of particle containing systems, it was shown that the influence of the particles depended upon the relative magnitudes of the stored energy of deformation and the particle-matrix interfacial energy. The particles effectively pinned the recrystallized boundaries at low values of stored energy, whereas beyond a certain critical stored energy the recrystallized boundaries swept through the particles. The simulations also predicted the occurrence of abnormal grain growth at small volume fraction of particles, when the stored energy of deformation was below the critical value for particle pinning. The deviation from ideal JMAK behavior displayed by real materials due to non-uniform stored energy was introduced in MC simulations [18] by varying the stored energy of a site as a function of its orientation number, thus resulting in a range of stored energy values for the cold-worked sites. The simulations showed significant deviations from ideal JMAK kinetics, as is commonly observed in real materials.

The distribution of stored energy in the MC recrystallization simulations was based on qualitative assumptions due to the lack of quantitative data on deformed microstructures. The representation of the grain orientations was again qualitative, since orientation numbers rather than true crystallographic axis-angle pairs were used in the simulations, which precluded the treatment of important microstructural features that evolve during cold deformation, such as the orientation differences within a grain arising from the inhomogeneous deformation of individual grains. As described later, these orientation differences are important in determining the potential for nucleation, both at the intergranular and intragranular sites in the deformed microstructure. A complete description of the crystallographic orientation of the sites also permits the simulation of

texture evolution during recrystallization. Finally, none of the previous MC simulations has explicitly modeled the nucleation process. Rather, the nuclei were arbitrarily placed in the microstructure based on certain simple rules. The current simulations provide, for the first time, a microstructural basis for the nucleation process based on subgrain growth in an orientation gradient.

The current article is a sequel to an earlier paper [20] which dealt with the finite element modeling of microstructural deformation using a crystal plasticity approach. The discretization of the grain structure at the level of each grain successfully captured the inhomogeneity of deformation from grain to grain as well as within a grain, thus providing a quantitative description of the cold-worked microstructure in terms of the grain orientations, and the distribution of the stored energy of deformation. In this article, the coupling of the cold deformation modeling with the MC simulation of recrystallization is described. The temporal evolution of the recrystallized microstructure and the recrystallization kinetics are simulated for two levels of cold work. A nucleation model based on subgrain growth in an orientation gradient is coupled with the MC recrystallization model so that the spatial distribution and the orientations of the recrystallized nuclei are obtained based on the evolution of the cold-worked microstructure rather than on arbitrary assumptions. The occurrence of simultaneous recovery during recrystallization is modeled based on the substructure evolution at each MC site. The deviation from JMAK kinetics, and the factors responsible for the deviation, such as non-random nucleation, anisotropic growth, etc., are discussed in detail.

Section 2 describes the procedure used for mapping the cold-worked microstructure to a MC grid. Section 3 describes the MC recrystallization model, along with the nucleation and recovery models. Section 4 provides the results of recrystallization simulations for plane strain deformations to plastic strains of $\varepsilon = 0.7$ and $\varepsilon = 1.1$. Section 5 is devoted to the discussion of the simulation results shown in section 4, with emphasis on the effect of prior cold deformation on the nuclei distribution, growth velocity, and the evolution of

recrystallized microstructure and texture. The important conclusions drawn from these simulations are summarized in section 6.

2 Mapping of Cold Worked Microstructure to MC Grid

The initial step in the simulations is to map stored energy and orientation distribution information from the deformed finite element (FE) mesh to a regular MC grid. In the current MC simulations, a cubic grid consisting of $30 \times 30 \times 30$ points was used. There are several ways of transferring the information from the FE mesh to the MC grid points, the most rigorous of which is to superimpose a regular, three-dimensional cubic mesh on the deformed volume, identify the element in which each MC site falls, and then assign the stored energy and orientation of the element to the MC site. However, in the current simulations, the mapping is carried out in a simplistic fashion which eliminates the necessity for such a superimposition technique.

It is assumed that the finite element mesh after a given deformation consists of elements which are elongated uniformly in the x direction and compressed uniformly in the z direction according to the overall deformation. For example, after plane strain compression to $\varepsilon = 0.7$, which corresponds to a reduction in height of 50%, a $15 \times 30 \times 60$ mesh consisting of 15, 30 and 60 cubic elements in the x, y and z directions, respectively, becomes a $30 \times 30 \times 30$ volume with the aspect ratios of the elements changed according to the overall deformation. Since the x direction has only 15 elements and 30 stored energy and orientation values are required in the x direction for the MC mesh, two equally spaced sites are chosen for each element with identical stored energy and orientation values. In the z direction, there are 60 elements while only 30 values are needed for the MC mesh. Here, the orientation and stored energy values of alternate elements are used. In a similar fashion for $\varepsilon = 1.1$, three points are chosen per element in the x-direction

and the orientation and stored energy of every third element is chosen in the z direction.

The current scheme used for mapping has certain limitations. First, the deformations of the elements are quite non-uniform compared to the overall deformation of the solid, especially in regions where a deformation band passes through the matrix of a large grain, or at certain grain boundary and triple point locations. Second, the methodology when extended to larger deformations, will result in the skipping of too many elemental values of stored energy and orientation in the z direction, and hence may not reproduce critical orientation gradients in the material. However, the method used here was deemed adequate for the purpose of illustrating the coupling between the deformation and recrystallization simulations. The simulations clearly demonstrate the impact of the cold-worked microstructure on the recrystallization process.

3 Monte Carlo Recrystallization Model

This section describes the Monte Carlo recrystallization model that was used in the current simulations. The MC simulations were carried out using a $30 \times 30 \times 30$ cubic lattice, which contained the orientation and stored energy distributions from the cold-worked microstructure obtained using the mapping technique described in the previous section. A unique feature of the MC recrystallization simulations used in the current research is the incorporation of a model for the nucleation of recrystallized grains. The nucleation model was fully coupled with the recrystallization simulation so that the two processes occurred simultaneously.

At this point, it is worthwhile to consider the difference between nucleation in the classical sense of atomic clustering and the nucleation phenomenon in recrystallization. In classical nucleation associated with phase transformations, where the critical nucleus size is only of the order of a few nanometers, there is a finite probability for the energy of the atom cluster to increase before the critical nucleus size is exceeded. However

in recrystallization, where the observed nucleus size is of the order of a micron, it is unlikely that activated states with greater energy could be sustained over such a large volume [21]. Therefore, the atomic processes that lead to the formation of a nucleus should result in a monotonic reduction in the overall energy. In recrystallization, the heterogeneous evolution of the subgrain structure is considered to be one of the main mechanisms for nucleation. The stored energy of cold work per unit volume, H, can be represented as [6],

$$H = \frac{2\gamma}{D}, \tag{6}$$

where D is the mean subgrain size and γ is the energy per unit area of a subgrain boundary given by

$$\gamma = \begin{cases} \gamma_m \frac{\theta}{\theta^*} \left[1 - \ln\left(\frac{\theta}{\theta^*}\right)\right] & \text{when } \theta \leq \theta^*, \\ \gamma_m & \text{when } \theta > \theta^*, \end{cases} \tag{7}$$

where θ is the misorientation bewteen two subgrains, γ_m is energy per unit area of a high-angle boundary, and θ^* is the misorientation limit for low angle boundaries, which is usually taken as 15°. The value of γ_m is taken to be 0.324 J/m^2, which is a typical value for high angle grain boundaries in Al. The stored energy per unit volume, H, varies from site to site. From FE simulations, H was found to vary from 1.75×10^5 to 2.41×10^5 J/m^3 for deformation to $\varepsilon = 0.7$. During subgrain growth, D increases and hence H decreases provided γ remains constant. However, γ is a function of the misorientation as shown in equation (7). If during subgrain growth the misorientation increases then γ increases until the misorientation reaches θ^*, beyond which it remains constant. Hence, for low angle boundaries the increase in specific boundary energy may exceed the decrease in energy associated with the reduction in the total boundary area. If the net energy change remains positive over a length scale of the order of a recrystallization nucleus then the nuclei will probably not form at such locations. The evolution of the subgrain

misorientation depends upon the local orientation distribution of subgrains in a region.

In the current simulations, each MC site was assigned a physical size such that it contained several subgrains. Also, for the range of subgrain mobilities used in the simulations, the MC site size had to be set such that there was no intermediate increase in the stored energy of the site during subgrain growth as discussed above. The size of the MC sites used in the current simulations was 20 μm. The site size was kept constant for both levels of cold work, so that direct comparison of the effect of cold work on recrystallization kinetics and microstructural evolution could be made. Periodic boundary conditions are used for the recrystallization simulation. However, nucleation simulation involves the calculation of average misorientation of a site with its nearest neighbors. Due to the use of periodic boundary conditions, the sites on the faces, edges and corners of the simulation domain were not considered for nucleation simulation.

In the MC simulation, the sites are visited in a random manner. At each site, one of the six first-nearest-neighbor sites is selected in a random manner. If the visited site is a cold-worked site, and the randomly selected nearest-neighbor site is also a cold-worked site, then the substructure at the current site is evolved based on analytical expressions that describe subgrain growth, and the possibility of nucleation is examined. If the formation of a nucleus at the site is not favored, then the site energy is updated to account for the loss of stored energy due to recovery. On the other hand, if the randomly selected nearest-neighbor site is a recrystallized site, then the possibility of changing the visited site into a recrystallized site is considered by calculating the local energy change as a result of converting it into a recrystallized site with the same orientation as the chosen recrystallized neighbor site. The local energy change, ΔE, is calculated as $E_{fin} - E_{init}$, where E_{init} is the initial energy and E_{fin} is the final energy after the flip. The initial energy is given by

$$E_{init} = \frac{4}{3}\pi L^3 H + \frac{2}{3}\pi L^2 \sum_i J_i, \tag{8}$$

where L is the radius of the MC site, J_i is the specific boundary energy between the site

and its i^{th} neighbor, which is a function of the misorientation between the two sites, as in equation (7). The misorientation, θ, is calculated using the axis-angle pairs for the two sites [20]. The final energy is given by

$$E_{fin} = \frac{2}{3}\pi L^2 \sum_i J_i', \tag{9}$$

where J_i' is the orientation dependent specific boundary energy between the i^{th} neighbor and the recrystallized site.

The reorientation of the visited site is allowed only when the local energy change ΔE is negative. However, the reorientation is effected with a probability which is a function of the orientation-dependent boundary mobility, k, given by [22]

$$\frac{k}{M} = M_{min} + (1 - M_{min}) \left[1 - \exp(-q\theta^3)\right], \tag{10}$$

where M is the high angle grain boundary mobility. In the above equation, M_{min} and q were taken to be 0.001 and 0.002, respectively [22]. When the local energy change is positive, the current site cannot be changed into a recrystallized site, and hence, the only process that is allowed is the continued evolution of the substructure at the current site. As before, the subgrain growth model is applied to the site, and the site energy is updated to account for the loss of stored energy due to recovery. If the visited site is already a recrystallized site, the two possibilities are that the randomly selected nearest neighbor site is a recrystallized site or a cold-worked site. If the selected neighbor site is cold-worked, then it corresponds to the case where a recrystallized site is attempting to change into a cold-worked site, which is not possible. If the selected site is also a recrystallized site, then the visited site can change into the selected site if the local energy change based on curvature change is negative. However, in the present calculations, the curvature-driven migration of boundaries between two recrystallized grains is ignored and only the migration associated with recrystallization is simulated. Hence, in the MC

simulations, when the visited site is a recrystallized site, it is ignored and the next MC site is accessed randomly. The flow chart of the MC algorithm is shown in Figure 1.

3.1 Nucleation Model

The nucleation model is based on subgrain growth in an orientation gradient. It is assumed that each MC site has a certain initial substructure characterized by a given mean subgrain size, D_0, and a mean misorientation between the subgrains, θ_0. The stored energy per unit volume, H, is related to D_0 and θ_0 as [6]

$$H = \frac{2\gamma_m}{D_0}\frac{\theta_0}{\theta^*}\left[1 - \ln\left(\frac{\theta_0}{\theta^*}\right)\right]. \tag{11}$$

Gil Sevillano *et al.* [23] have carried out an extensive characterization for the substructure of various pure metals deformed in compression to different strain levels. Vatne *et al.* [24] have fitted an analytical expression to the experimental results of Gil Sevillano *et al.* [23] as

$$D_0 = 3.5 \times 10^{-7} + \frac{1.7 \times 10^{-7}}{\varepsilon}, \tag{12}$$

where D_0 is the subgrain size in meters. Equation (12) was used to assign a mean initial subgrain size to each MC site, which was based on the local effective plastic strain for the site obtained using the polycrystal deformation model. The initial misorientation, θ_0, was then calculated from equation (11), from the known value of H. The misorientation limit for low angle boundaries, θ^*, is assumed to be 15° in the present simulations.

The subgrain growth at each MC site is modeled on the basis of curvature-driven growth using the growth law given by [6]

$$\frac{dD}{dt} = \frac{k}{D}, \tag{13}$$

where k is the mobility of the subgrain boundary given by equation (10).

However, the evolution of the subgrain structure can also be due to abnormal growth of the subgrains, that occurs when certain microstructural and grain boundary features are satisfied [25]. The abnormal grain growth model is currently being incorporated into the recrystallization model and will form the subject of a later publication.

During normal growth, if the subgrains grow in a region over which they are randomly oriented in space, then the mean misorientation between subgrains will fluctuate randomly. Hence, irrespective of the mean subgrain size, the misorientation between the subgrains can never exceed the critical low angle limit of 15°. On the other hand, if the subgrains grow in a region where there is a large orientation gradient, then the mean misorientation between the subgrains will monotonically increase during subgrain growth. In this case it is possible to exceed the critical low angle limit fairly quickly, and hence it is possible to create mobile high angle boundaries. The growth rate of subgrains in such a region will also be greater since the mean subgrain mobility also increases systematically with subgrain size according to equation (13).

Equation (13) by itself does not fully quantify how the misorientation between the subgrains will change during subgrain growth at each MC site. Hence, we need another expression which links the misorientation between subgrains at a given MC site to the mesoscopic orientation gradient that exists in the cold-worked material at the different MC sites. Such a link is provided by the following equation,

$$\frac{\theta - \theta_0}{D - D_0} = \frac{\theta_{av} - \theta_0}{2L - D_0}, \tag{14}$$

where θ_{av} is half the average misorientation between a given MC site and its nearest neighbors. Equation (14) assumes that as the subgrains grow, the mean misorientation between the subgrains at a given site varies linearly with the average misorientation between the site and its nearest neighbors. The misorientation between the subgrains becomes equal to half the average misorientation between the site and its nearest neigh-

bors when the subgrains grow heterogeneously and the mean subgrain size reaches the size of the MC site. Equations (13) and (14) can be solved in a coupled fashion to determine both the mean subgrain size, D, and the mean misorientation between the subgrains, θ, at the site at any given time. In the current simulations, a given MC site is declared as a nucleus when the mean misorientation between the subgrains exceeds the critical value of 15°. It is important to note that the subgrain size at which a high angle boundary is created varies from site to site, since both the stored energy and the misorientation with nearest neighbors, $2\theta_{av}$, are site-dependent.

According to the above nucleation model, the two quantities which determine the nucleation potential at a given MC site are the stored energy per unit volume and the misorientation between the site and its neighbors. The higher the stored energy per unit volume, the smaller is the mean subgrain size, D_0, and larger is the mean misorientation between the subgrains at the site, θ_0. Therefore, the initial growth rate of the subgrains increases with the stored energy. The large misorientation between the site and its nearest neighbors provides the orientation gradient required for creating a high angle boundary during subgrain growth. It is possible to define a nucleation parameter, ν, which is the product of the stored energy per unit volume and the average misorientation between the site and its surroundings.

3.2 Modeling of Recovery

As described previously, the energy of the MC sites has to be updated for two cases. The first case corresponds to the reorientation attempt of a cold-worked site to another cold-worked site. The only microstructural event that is allowed during this time is the growth of the subgrains. If the misorientation of the subgrains has not yet reached the critical limit for the site to be declared a nucleus, then the energy of the site is updated using the current values of the mean subgrain size, D, and the mean subgrain misorientation, θ, in equations (6) and (7). The second case corresponds to an unsuccessful

reorientation attempt of a cold-worked site to a recrystallized site. Since the recrystallization front does not sweep through the cold-worked site due to a lack of driving force, the microstructural event that can occur in the cold-worked site is again a continued coarsening of the subgrains, and hence its energy has to be updated as before.

4 Results

The above MC recrystallization methodology was applied to the cold-worked fcc microstructures obtained using FE simulations [20]. Figure 2(a) shows the recrystallization fraction as a function of the simulation time expressed as Monte Carlo Step (MCS) after plastic strains of $\varepsilon = 0.7$ and 1.1. It is clear that the greater amount of cold work resulted in faster recrystallization kinetics. While the recrystallization is essentially complete for $\varepsilon = 1.1$, the recrystallization fraction appears to level off at an f_{rex} of about 0.9 for $\varepsilon = 0.7$. Figure 2(b) shows a plot of $\ln[\ln\{1/(1-f_{rex})\}]$ as a function of ln(MCS) for the data shown in Fig. 2(a). For ideal JMAK behavior, the plot shown in Fig. 2(b) should be a straight line. However, Fig. 2(b) shows significant deviations from ideal JMAK behavior, seen as a decrease in the slope of the curve at higher recrystallization volume fractions.

Figure 3(a) shows the evolution of the surface energy per unit volume (S_v) of the boundaries between the recrystallized and unrecrystallized portions of the microstructure. S_v initially increases with f_{rex} before reaching a maximum and then decreasing to zero when the recrystallization is complete. There are significant differences in the variation of S_v with f_{rex} for $\varepsilon = 0.7$ and $\varepsilon = 1.1$. For the lower plastic strain, S_v attains a maximum value of 0.35 at an f_{rex} of 0.33, while for $\varepsilon = 1.1$ the maximum S_v is 0.5 at an f_{rex} of 0.42. This results in the S_v curve being asymmetric for $\varepsilon = 0.7$, with a sharp ascent followed by a more gradual decline, while the curve for $\varepsilon = 1.1$ is more symmetrical.

Figure 3(b) shows the derivative of f_{rex} with respect to MCS as a function of f_{rex}. It can be seen that the f_{rex} values at which S_v reaches maximum values in Fig. 3(a) correspond to the points of inflexion in the f_{rex} versus MCS curves shown in Fig. 2(a).

Figures 3(a) and 3(b) also show the S_v and the derivative of f_{rex} with respect to MCS, respectively, for the case where the stored energy loss due to recovery was not taken into account. It can be seen that the reduction of driving force due to recovery can also cause an asymmetry in these curves. The role of recovery in reducing the driving force for recrystallization will be discussed later.

Figures 4(a) and 4(b) show the total number of recrystallization nuclei as a function of MCS and fraction recrystallized, respectively, for the two plastic strains. Both the nucleation rate and the total number of nuclei increase with the extent of plastic strain. The total number of nuclei for $\varepsilon = 1.1$ is about 900, while it is about 500 for $\varepsilon = 0.7$. The nucleation rate becomes negligible at MCS approximately equal to 11 for both $\varepsilon = 0.7$ and $\varepsilon = 1.1$. This corresponds to recrystallization fractions of approximately 0.3 and 0.4, respectively for the two plastic strains, from Fig. 2(a). From Fig. 3(a), it can be seen that these volume fractions approximately correspond to those at which the respective S_v curves also go through a maximum. Figure 4(b) also shows the number of nuclei as a function of fraction recrystallized, when the loss of stored energy due to recovery was not taken into account. In other words, the subgrain growth model was used in this case only to model the nuclei formation, and not the evolution of the stored energy. The purpose of this simulation is to model the recrystallization kinetics in the absence of recovery, and to determine the role played by recovery during recrystallization.

Figures 5 and 6 show the mean velocity of the recrystallization front, G, as a function of the recrystallized fraction and MCS respectively, obtained by using the Cahn-Hagel relationship [26] given by

$$G = \left[\frac{df_{rex}/dt}{S_v} \right]_{f_{rex}} . \tag{15}$$

These figures also show the corresponding recrystallization velocities when the reduction

of driving force due to recovery was not taken into the recrystallization model. At any given f_{rex}, the mean velocity of the recrystallization front is seen to be higher for $\varepsilon = 1.1$. Figure 5 also shows that the recrystallization velocity for $\varepsilon = 0.7$ decays more quickly than that for $\varepsilon = 1.1$. The decay in recrystallization velocity due to recovery is seen clearly, in both Fig. 5 and Fig. 6. However, the recrystallization velocity as a function of MCS is also seen to decrease significantly in the absence of recovery. The reason for this behavior will be discussed later.

Figures 7 and 8 show the recrystallization kinetics and the evolution of the S_v for the two plastic strains, assuming different values for the grain boundary mobility, k, shown in equation (10). Increasing the subgrain mobility makes the nucleation more non-random and the impingement of the recrystallization fronts occurs at lower recrystallized fractions. The kinetics of recovery also increases with increasing k resulting in incomplete recrystallization for both cold work levels.

As described previously, each MC site in the initial microstructure was represented by a rotation angle and a rotation axis with respect to a reference frame. Hence, a complete representation of the initial orientations in the microstructure would require separate plots of the grain structure using the rotation angle, ω, as well as each of the three direction cosines of the rotation axis, $\boldsymbol{c}$, using a color scheme. Figures 9(a) and 9(b) show a schematic of the deformed microstructure for a plastic strain of $\varepsilon = 0.7$ obtained by mapping the initial $15 \times 30 \times 60$ volume to a $30 \times 30 \times 30$ cube, plotted using initial c_x and initial ω, respectively, where c_x is the direction cosine of the rotation axis with respect to the reference x-axis. The two plots taken together provide sufficient contrast to distinguish all the grains in the microstructure. Figures 9(c) and 9(d) show the actual deformed grain structure using the same color scales used in Figs 9(a) and 9(b), respectively. By comparing Figs 9(a) and 9(c), and 9(b) and 9(d), the evolution of c_x and ω, respectively, with deformation can be seen clearly. It is seen that deformation is accompanied by grain rotations which vary not only from grain to grain but also within

a grain. A similar intergranular and intragranular heterogeneity is also obtained for the stored energy of deformation, as shown in Fig. 9(e). Figure 9(f) shows the distribution of the nucleation parameter for the section shown in Figs 9(a–d). Examining Figs 9(a) and 9(f), it is clear that the nucleation parameter is very high at certain grain boundary and triple point locations. Figure 9(f) also shows the existence of a band of sites with very high values for the nucleation parameter going across the grain marked "a" in Fig. 9(a). An analysis of the deformation of the FEM mesh [20] indicates that it could be a transition band. Close examination of various sections of the deformed volume indicated several occurrences of such bands going through the grains, with high values for the nucleation parameter in some of the bands. Figures 10(a–f) show the deformed microstructure, the stored energy distribution and the distribution of the nucleation parameter for plastic strain of 1.1. From Figs 9(f) and 10(f), it is seen that the nucleation parameter is distributed more uniformly for $\varepsilon = 1.1$ than for $\varepsilon = 0.7$.

Figure 11 shows the temporal evolution of the recrystallized microstructure for $\varepsilon = 0.7$. Notice that there is a one-to-one correlation between the sites at which the nucleation parameter has high values (see Fig. 9(f)) and the sites at which the initial nuclei form. Since the nucleation parameter is not randomly distributed, the nucleation also occurs in a non-random fashion. The growth of the non-randomly distributed nuclei results in an early impingement of the recrystallized grains as shown in Fig. 11 at MCS = 13. There is no further nucleation beyond this point as shown in Figs 11 and 4(a). In fact, the unrecrystallized regions shown in Fig. 11 do not recrystallize further and evolve only through a recovery process. Figure 12 shows the evolution of the recrystallized microstructure for $\varepsilon = 1.1$. Notice that the more random distribution of the nucleation parameter causes the nucleation to also occur in a random fashion. The more uniform impingement of the recrystallized grains leads to a complete recrystallization, although the recrystallization kinetics are again retarded after significant impingement of the existing nuclei.

Figure 13 shows the temporal evolution of recrystallized microstructure for $\varepsilon = 0.7$ when the reduction in stored energy due to simultaneous recovery is not taken into account. Although the initial nucleation and growth are very similar to those shown in Fig. 11 up to MCS=13, the extent of overlap of the recrystallization fronts is significantly less at this point in the absence of recovery, and continued growth of the recrystallization fronts leads to complete recrystallization.

Figures 14 and 15 show the <111> pole figures of the cold-worked microstructure, recrystallized nuclei and the recrystallized microstructure for $\varepsilon = 0.7$ and 1.1, respectively. By comparing the pole figures of the cold-worked microstructure and the recrystallized nuclei, it can be seen that there is little correlation between the relative number densities of the nuclei orientations and the relative number densities of corresponding orientations of the deformed grains. The relative number density of nuclei is high in certain orientations where it was low in the as-deformed microstructure. Comparison of the pole figures for the deformed and the recrystallized microstructures in Figs 14 and 15 indicate that there is a significant redistribution of the grain orientations after recrystallization. No new orientations are created during recrystallization, but there are significant changes in the relative strengths of existing orientations.

5 Discussion

5.1 Nucleation Model

The coupling of the MC recrystallization simulation with the FEM microstructural deformation model based on crystal plasticity approach has resulted in a powerful approach for modeling recrystallization in a more fundamental sense than before. A unique feature of the recrystallization simulations is that for the first time, a fundamental nucleation model based on subgrain growth has been coupled with the actual environment of the cold-worked microstructure at the mesoscale. Previous studies of nucleation during re-

crystallization based on subgrain growth have stressed the importance of the long range orientation gradients in the formation of high angle boundaries [6, 10, 11, 21, 27]. However, the modeling of nuclei formation by subgrain growth in an orientation gradient has been handled only in an isolated sense using a qualitative assignment of stored energies and orientation gradients [10, 11]. The present study is the first of its kind in trying to implement such a model into a microstructural framework. The model provides a basis for predicting not only the spatial distribution of nuclei and its influence on the overall recrystallization kinetics, but also the evolution of the recrystallization texture.

The key to the coupling of the substructure evolution at any given location with the potential for nucleus formation is the assumption inherent in equation (14), which implies that the misorientation between the subgrains during growth will monotonically increase when the misorientation of the site with respect to the nearest neighbors is high.

The variation of the mean misorientation between subgrains and the mean subgrain size are shown as a function of simulation time in Fig. 16, for sites with low, medium and high values of the nucleation parameter, ν. Notice that the average misorientation remains more or less constant for the site with low ν, while it increases significantly for the site with high ν. The rate of growth of the subgrains is also higher for the site with high ν because of the higher mobility of the boundaries, thus showing that the subgrain growth occurs heterogeneously in the microstructure. For the high ν site shown in Fig. 16(b), the critical misorientation angle of 15° is reached fairly quickly. Beyond that point, the growth rate is governed by equation (13), with k=M, the mobility of high angle boundaries. The site is declared a nucleus when the mean subgrain misorientation exceeds 15°. It is important to note that for the sites with low and medium ν, the critical misorientation is never reached even after the mean subgrain size reaches the site size, indicating that continued recovery is the only possible softening mechanism, unless the site is swept by a moving recrystallization front.

The misorientation between a site and its nearest neighbors is related to the inho-

mogeneity of deformation between the site and its nearest neighbors. If a site and its nearest-neighbor sites are at the same orientation at the beginning of deformation, and go through the same path of deformation, the orientation gradient in the region will be small, as will the probability of nucleation. However, if the site and its neighbors are subjected to different levels of deformation through different deformation paths, then the average misorientation between the site and the nearest neighbor sites will be significantly higher for the same level of overall deformation. In such a case, according to equations (13) and (14), the misorientation between the subgrains will monotonically increase and exceed the critical low angle limit of 15°. The inhomogeneity of deformation at the grain boundary and triple point sites and at intragranular sites associated with the deformation bands provides the large orientation gradients required for nucleation.

5.2 Microstructural Path of Recrystallization

The microstructural path of recrystallization is best explained by the shape of the S_v curves shown in Fig. 3(a) for the two plastic strains. The initial increase in the S_v corresponds to the period where the recrystallized nuclei form and continue to grow freely in all the three principal directions. Beyond a certain point, the recrystallization fronts from different regions start to overlap and hence there is a loss of surface area between the recrystallized and the unrecrystallized regions. The S_v continues to increase while the increase in the surface area due to recrystallization is greater than the loss of surface area due to overlap. The point at which S_v reaches a maximum depends on three factors—the spatial distribution of the nucleation sites, the rate of nucleation, and the local anisotropy in the growth rates of the recrystallization fronts.

In the present simulations, the non-random distribution of the nucleation sites and the non-random impingement of the recrystallization fronts originating from these sites lead to the asymmetry observed in the S_v curves. The asymmetry is more significant for $\varepsilon = 0.7$ than for $\varepsilon = 1.1$ as evidenced by the more non-random distribution of the

nucleation sites in the former than latter, as seen from Figs 3(a), 9 and 10. The maximum in the S_v curve for both the plastic strains corresponds to the point at which the impingement from adjacent recrystallization fronts is complete, which is a little after the respective nucleation rates go to zero. The nucleation rate also controls the point at which S_v reaches its maximum, since delayed nucleation at late stages of recrystallization can increase S_v. However, no such delayed nucleation was found in the present simulations.

From Fig. 4(b), it can be seen that the number of nuclei as a function of f_{rex} does not change significantly when the reduction in recrystallization kinetics due to recovery of stored energy is not considered. Since nuclei essentially form at the same locations where the nucleation probability is high, the spatial distribution of nuclei does not change significantly. However, the S_v versus f_{rex} curve shown in Fig. 3(a) has become more symmetrical in the absence of recovery effects, in spite of the non-random distribution of nuclei. This is essentially due to changes in the local anisotropy of growth of recrystallization fronts due to recovery. By comparing Figs 11 and 13 it is clear that the non-random distribution of the recrystallization fronts is approximately the same with and without recovery effects until MCS=13. However, when the recovery effects are absent, there is an additional growth front in the upper portion of Fig. 13 (colored green) which is absent in Fig. 11. This is because in the presence of recovery, the growth of the corresponding nucleus in the z-direction is arrested by the loss of driving force, and growth is possible only in the x-direction. The presence of the additional recrystallization front in the absence of recovery allows the continued increase in the S_v until overlap occurs at higher recrystallized fraction. From Figs 11 and 13 it can be seen that the shapes of the recrystallized grains with and without recovery are significantly different for many of the recrystallized grains, indicating that the recovery plays a significant role in changing the local anisotropy of growth.

5.3 Recrystallization Velocity

The growth velocity of a recrystallization front, G, can be expressed as

$$G = kF, \tag{16}$$

where k is the boundary mobility given by equation (10), and F is the driving force. During recrystallization, the velocity can change if the boundary mobility and/or the driving force changes. The change of driving force is due to the occurrence of simultaneous recovery and/or the non-uniform distribution of stored energy of deformation. The recrystallization velocity also depends on the boundary mobility which varies with the boundary misorientation as in equation (10).

The occurrence of recovery during recrystallization reduces the driving force by reducing the stored energy of deformation and causes a reduction in the boundary velocity. Figure 17 shows the stored energy of sites with low, medium and high values for the nucleation parameter, ν, as a function of MCS. Notice that the drop in the stored energy due to recovery is very rapid at early recrystallization times and decays more slowly at longer recrystallization times. There have been several instances where the observed recrystallization velocity decreased as function of recrystallization, which was attributed to recovery effects [28–30]. A similar decrease in recrystallization velocity due to non-uniform stored energy of distribution can also occur if the first regions to recrystallize are those with the highest stored energy. This has been reported in systems with low stacking fault energy (SFE), where significant recovery by cross-slip of dislocations does not occur [6]. In fact, it has been shown [31, 32] that even for systems with high SFE in which significant recovery can occur, prior recovery treatments do not have a significant effect on the recrystallization kinetics, and the observed deviation from ideal JMAK kinetics indicates that the reduction in recrystallization velocity is probably due to the non-uniform stored energy distribution rather than recovery.

The reduction in driving force leads to a reduction in the recrystallization velocity with time given by

$$G = \frac{A}{1 + Bt^g}, \tag{17}$$

where A and B are constants [6]. At long times, G reduces to equation (5). Values of g close to 1.0 have been found in many cases [6], although in one instance, g was found to be 0.38 [7].

In equation (17), A is the recrystallization velocity at $t = t_0$, the time corresponding to the constant, steady state velocity shown in Fig. 6 in the absence of recovery. The initial high recrystallization velocity shown in Fig. 6 is an artifact of the methodology used to obtain the velocity and is not representative of the physical phenomenon. Assuming $A = 0.26$ at $t = t_0$, the recrystallization velocity versus MCS curves shown in Fig. 6 were fitted to an equation of the form shown in equation (17). The exponent g was found to be 1.77 for $\varepsilon = 0.7$ and 2.18 for $\varepsilon = 1.1$. These values, although high compared to those mentioned above, are in good agreement with that found for high-purity aluminum deformed 40% by channel die compression [8], where an exponent of 1.9 was found. It is significant to note that the above g values of 1.77 and 2.18 obtained in these simulations include the effects due to recovery, non-uniform stored energy distribution, and the mobility variation due to variation in the boundary misorientation during recrystallization.

In the absence of recovery, the recrystallization velocity remains constant until a certain recrystallization volume fraction is reached, as opposed to the continuous drop in velocity observed in the presence of recovery. The recrystallized fraction at which the steady state velocity begins to drop is higher for $\varepsilon = 1.1$ than for $\varepsilon = 0.7$, as seen from Fig. 5.

The drop in the recrystallization velocity in the absence of recovery is mainly due to the mobility effect described above. This effect is seen clearly only when the recovery effect is removed since it is a much smaller effect which occurs only at high f_{rex} values. In

the initial stages of recrystallization, all the regions having high misorientation with the recrystallization fronts are consumed first, so that in the final stages of recrystallization only the regions with smaller misorientations remain. By turning off the mobility effect completely, it was seen that the steady- state recrystallization velocity remained constant until complete recrystallization occurred.

5.4 Deviation from JMAK Kinetics

For ideal JMAK kinetics, the plots shown in Fig. 2(b) should be straight lines, with the slopes giving the corresponding JMAK exponents. In the current simulations, the deviation from ideal JMAK behavior is indicated by significant changes in the JMAK exponent with recrystallized fraction, as shown in Fig. 2(b). The curves are characterized by three main stages of recrystallization. In the first stage the JMAK exponent is rather high, with values ranging from about 7.0 to about 4.0. The final stage of the curve is characterized by a significantly lower JMAK exponent of 0.85. The two stages are separated by a transition stage where the JMAK exponent changes from about 4.0 to 0.85. One of the causes for the deviation from ideal JMAK kinetics could be the variation of the nucleation and growth rates during recrystallization.

For the final stage of recrystallization the JMAK exponent is 0.85, and the exponent m is zero since the nucleation rate is zero. Application of equation (3) suggests that g should be 1.05 for $\varepsilon = 0.7$ and $\varepsilon = 1.1$. However, g values of 1.77 and 2.18 were obtained in the current simulations, for $\varepsilon = 1.1$ and $\varepsilon = 0.7$, respectively. Hence, it is clear that the JMAK analysis does not explain the observed recrystallization kinetics. It should be emphasized that the derivation of equation (3) has the assumptions that the growth is isotropic and that the nuclei are distributed randomly in the recrystallizing volume, both of which are not true in the current simulations. From Figs 11 and 12 it is clear that the nucleation of recrystallization is non-random. A careful observation of grain shapes in Figs 11 and 12 indicates that not all grains are equiaxed. There are many

grains which are elongated either in the x- or z-direction, indicating local anisotropy of growth. The local velocity of the recrystallization front depends on the local driving force which is clearly a variable in the present simulations.

5.5 Effect of Prior Deformation

It is well known that higher deformation prior to recrystallization results in faster recrystallization kinetics. This has been attributed to the increased level of stored energy at higher deformations, thus providing a greater driving force for recrystallization as well as an increased nucleation rate. In the present simulations, the nucleation rate and the number of nuclei were found to increase with prior deformation, as shown in Figs 4(a) and 4(b). In the absence of recovery, the steady state recrystallization velocity for $\varepsilon = 1.1$ is higher than that for $\varepsilon = 0.7$ for any given f_{rex} or MCS as seen from Figs 5 and 6, indicating the availability of greater driving force. In the presence of recovery, the recrystallization velocities as a function of time do not vary significantly as seen in Fig. 6. This is because recovery tends to reduce the difference in the stored energies between $\varepsilon = 0.7$ and $\varepsilon = 1.1$. As seen from Fig. 17, the difference in driving force for the two prior cold work levels becomes negligible beyond MCS=30, for all sites. For MCS less than 30, only those sites with medium ν values appear to have higher stored energy values for $\varepsilon = 1.1$ than for $\varepsilon = 0.7$, while the stored energies of sites with low ν appear to be the same for both cold work levels. Hence, the recrystallization velocity in the presence of recovery for $\varepsilon = 1.1$ is only marginally higher than that for $\varepsilon = 0.7$. Beyond MCS=30, the two velocities are almost the same. The recrystallization velocity at a given f_{rex}, shown in Fig. 5 is significantly higher for $\varepsilon = 1.1$ because it corresponds to a shorter recrystallization time, and hence, less reduction in driving force than for $\varepsilon = 0.7$.

5.6 Recovery during Recrystallization

The extent of recovery that occurs during recrystallization is directly related to the kinetics of subgrain growth, which depends not only on the stored energy of deformation at a site but also on the evolution of the misorientation between the subgrains as they grow. As described previously, sites with a high stored energy are characterized by a small subgrain size and a high misorientation between subgrains (through equation (11)). Therefore, the initial growth rate of the subgrains is also high. Since the subgrain mobility is a function of the misorientation, the kinetics of subgrain growth will be high if the growth is accompanied by an increasing misorientation. Such a condition will be met at regions where there are long range orientation gradients. The growth kinetics, and hence recovery, are high at those locations where the nucleation parameter is also high. Hence, recovery plays a dual role in recrystallization. While it promotes nucleation by subgrain growth, it also slows down the recrystallization kinetics by reducing the driving force, especially in the early stages of recrystallization. The dual role of recovery is seen clearly in Figs 7 and 8, where increased recovery due to increased boundary mobility results in an acceleration of the recrystallization kinetics (through increased nucleation rate) in stage 1, whereas in stage 3, the kinetics becomes slower because increased recovery leads to reduction in stored energy, and hence, the driving force for recrystallization.

5.7 Evolution of Texture during Recrystallization

The nucleation model based on subgrain growth allows the prediction of nuclei orientations during recrystallization. Figs 14 and 15 show <111> pole figures of the cold-worked microstructure, recrystallized nuclei and the recrystallized microstructure for $\varepsilon = 0.7$ and $\varepsilon = 1.1$, respectively. While the cold-worked and the recrystallized textures are based on 27,000 orientations, the recrystallized nuclei are much smaller in number.

The orientation of a nucleus is the same as the orientation of the MC site where it is formed. For this reason, no new orientations are introduced during the recrystallization simulation. The cold-worked microstructure shows typical rolling texture components such as copper, S and brass [6]. Some of the orientations which have very low relative intensity levels appear among the nuclei, as seen from Fig. 14(b) and Fig. 15(b). These nuclei grow to varying sizes, and hence, their relative number densities also vary. This is reflected in the textures after recrystallization, where the same orientations exist but with different relative intensities. For the case of $\varepsilon = 0.7$, since recrystallization does not go to completion, some deformation components are also present albeit with much smaller intensities. Although some of the early models of nucleation proposed mechanisms such as twinning for the formation of apparently new orientations during recrystallization [33], it is now clear that these models are highly improbable and current models [8, 21, 34–36] are all based on the assumption that recrystallized nuclei already exist in the deformed microstructure.

Of particular significance is the formation of strong cube or rotated cube orientations from a cold-worked microstructure that apparently does not contain many of these orientations. Here again, there is a strong polarization between models which are based on oriented nucleation (ON) and those based on oriented growth (OG). According to the ON models, cube orientations have a particular advantage in forming the nuclei because of the large and long-range orientation gradients existing in their vicinity. However, the OG models are based on the assumption that nuclei occur randomly in the cold-worked microstructure, but the reason that the final texture has strong cube components is due to the high mobility of the cube oriented grains [37–40]. The controversy between the ON and OG proponents is still unresolved, probably due to the lack of quantitative understanding of the cold-worked microstructure in fcc materials.

A notable feature of the recrystallization textures in the present simulations is the lack of strong cube texture commonly observed in cold-rolled and annealed fcc mate-

rials. A careful analysis of the orientations in the cold-rolled microstructure indicated that only a few rotated cube orientations were present. This is in agreement with the experimental results of texture in high-purity Al deformed to 40% by channel die compression [8], where X-ray measurements showed no cube components. In fact, only after 95% deformation did the cube components appear in the X-ray measurements. Recent simulations by Beaudoin *et al.* [41] have also indicated the need for large strains in developing cube orientations in fcc materials.

In the current recrystallization simulations, one of the rotated cube orientations became a nucleus and grew to a grain size of approximately 4.67, for $\varepsilon = 0.7$. Hence, it is clear that the present simulations can potentially capture the formation of cube texture during cold working and annealing of fcc materials. However, the intensity of the cube texture obtained after recrystallization is quite negligible compared to the intensities of other orientations. This is again in agreement with the experimental results [8] where it was found that the 40% deformed Al had only one out of 30 grains analyzed which was in the cube orientation after recrystallization. In the current simulations, some of the rotated cube orientations in the cold-worked material were eliminated during the mapping of the cold-worked microstructure to the MC mesh, which also contributed to the observed low cube intensity after recrystallization. The loss of cube orientations was because the mapping involved the selection of one out of two elements in the z-direction for $\varepsilon = 0.7$ and one out of three elements for $\varepsilon = 1.1$. In the future, a more accurate method of mapping will be developed that does not result in the loss of orientations during mapping. Since the cube orientations are known to form preferentially in deformation bands, efficiently capturing all the orientations in a deformation band will also require better spatial resolution in the discretization of the grains than obtained in the current simulations.

6 Summary and Conclusions

A model for static recrystallization has been developed by coupling a FE deformation model based on crystal plasticity approach with a MC simulation of recrystallization. The FE model provides quantitative information on the cold-worked microstructure in terms of the grain orientations and the distribution of the stored energy of deformation. By transferring this information to a MC grid it has been possible to incorporate a nucleation model for recrystallization based on subgrain growth in an orientation gradient. The nucleation model provides a quantitative description of the orientations and spatial distribution of the nuclei. The subgrain growth model also allows the modeling of simultaneous recovery during recrystallization and the effect of recovery on the recrystallization kinetics. Since the orientations of the recrystallization nuclei can be predicted, the model provides a convenient tool for studying texture evolution during recrystallization.

The above model has been applied to the recrystallization of an fcc material after cold-work levels of $\varepsilon = 0.7$ and $\varepsilon = 1.1$ obtained by plane strain compression. The following conclusions are drawn based on the simulation results:

1. The total number of nuclei increased with prior cold-work, resulting in a finer recrystallized grain size as the prior cold work is increased.

2. For both cold work levels, the spatial distribution of nuclei is non-random, although the distribution becomes more random with increasing cold work. The non-random distribution of nuclei results in a non-random impingement of the recrystallization fronts, which results in a reduction in the dimensionality of growth, and hence a reduction in the recrystallization kinetics.

3. Increased nucleation rate, greater number of nuclei and more random spatial distribution of nuclei result in a faster recrystallization kinetics for a prior deformation of $\varepsilon = 1.1$ than for $\varepsilon = 0.7$.

4. Both non-random nucleation and anisotropic growth of nuclei lead to breakdown of the JMAK analysis of recrystallization, even after incorporating the effects of variable nucleation rate and growth rate on the JMAK exponent.

5. Recovery plays a dual role in recrystallization. While it increases the recrystallization kinetics in the initial stages by promoting nucleation by subgrain growth, it reduces the recrystallization kinetics at later stages by reducing the stored energy of deformation and hence the available driving force for recrystallization.

6. The coupled FE-MC model is capable of predicting the nucleation and growth of rotated cube components during the cold rolling and annealing of fcc materials. However, the intensity of the rotated cubes is weak. This is because of the lack of sufficient grain orientations in the initial microstructure, and the loss of orientations in the cold-worked material during the mapping process. Hence, a more rigorous mapping scheme than the one currently used in the simulations is required.

Acknowledgments

This research was sponsored by the Division of Materials Science, U.S. Department of Energy, under contract DE-AC05-96OR22464 with Lockheed Martin Energy Research Corporation. The research was supported in part by an appointment to the Oak Ridge National Laboratory Postdoctoral Research Associates Program administered jointly by the Oak Ridge National Laboratory and the Oak Ridge Institute for Science and Education. The authors acknowledge the use of the Intel PARAGON XP/S 35 located in the Oak Ridge National Laboratory Center for Computational Sciences (CCS), funded by the Department of Energy's Office of Scientific Computing.

References

[1] D. Hull and D. J. Bacon, *Introduction to Dislocations.* Pergamon Press, Oxford (1984).

[2] D. A. Hughes, *Microstructural and Crystallographic Aspects of Recrystallization*, 16th Risø International Symposium on Materials Science, p. 63. Roskilde, Denmark (1995).

[3] D. A. Hughes, Q. Liu, D. C. Chrzan and H. Q. Ye, *Acta metall.* **45,** 125 (1997).

[4] G. S. Rosen, D. Juul-Jensen, D. A. Hughes, and N. Hansen, *Acta metall.* **43,** 2563 (1995).

[5] R. J. Asaro, *Advances in Applied Mechanics, Volume 23.* Academic Press (1983).

[6] F. J. Humphreys and M. Hatherly, *Recrystallization and Related Annealing Phenomena.* Elsevier Science Ltd., Oxford (1995).

[7] R. A. Vandermeer and B. B. Rath, *Metall. Trans. A* **20,** 391 (1989).

[8] R. D. Doherty, K. Kashyap and S. Panchanadeeswaran, *Acta metall.* **41,** 3029 (1993).

[9] H. V. Atkinson, *Acta metall.* **36,** 469 (1988).

[10] F. J. Humphreys, *Mater. Sci. and Tech.* **8,** 135 (1992).

[11] F. J. Humphreys, *Scripta Metall.* **27,** 1557 (1992).

[12] T. Saetre, O. Hunderi and E. Nes, *Acta metall.* **34,** 981 (1986).

[13] K. Marthinsen, O. Lohne and E. Nes, *Acta metall.* **37,** 115 (1989).

[14] T. Furu, K. Marthinsen, and E. Nes, *Mater. Sci. Tech.* **6,** 1093 (1990).

[15] D. J. Srolovitz, G. S. Grest and M. P. Anderson, *Acta metall.* **34,** 1833 (1986).

[16] D. J. Srolovitz, G. S. Grest, M. P. Anderson and A. D. Rollett, *Acta metall.* **36,** 2115 (1988).

[17] A. D. Rollett, D. J. Srolovitz, M. P. Anderson and R. D. Doherty, *Acta metall.* **40,** 3475 (1992).

[18] A. D. Rollett, D. J. Srolovitz, R. D. Doherty and M. P. Anderson, *Acta metall.* **37,** 627 (1989).

[19] H. W. Hesselbarth and I. R. Gobel, *Acta metall.* **39,** 2135 (1991).

[20] G. B. Sarma, B. Radhakrishnan and T. Zacharia, submitted to *Computational Materials Science.*

[21] R. D. Doherty, I. Samajdar, C. T. Necker, and H. E. Vatne *Microstructural and Crystallographic Aspects of Recrystallization*, 16th Risø International Symposium on Materials Science, p. 1. Roskilde, Denmark (1995).

[22] A. D. Rollett and E. A. Holm, presented at the *International Conference on Recrystallization and Related Topics*, Monterey, CA, October 21-24 (1996).

[23] J. Gil Sevillano, P. van Houtte, and E. Aernoudt, *Progress in Mater. Science* **25,** 69 (1980).

[24] H. E. Vatne, T. Furu and E. Nes, presented at the *International Conference on Recrystallization and Related Topics*, Monterey, CA, October 21-24 (1996).

[25] A. D. Rollett, D. J. Srolovitz and M. P. Anderson, *Acta metall.* **37,** 1227 (1989).

[26] J. W. Cahn and W. Hagel, *Decomposition of Austenite by Diffusional Processes* (edited by V. F. Zackay and H. I. Aaronson), p. 131. Interscience, New York (1960).

[27] M. Ferry and F. J. Humphreys, *Acta metall.* **44,** 1293 (1996).

[28] R. A. Vandermeer and P. Gordon, *Trans. Metall. Soc. A.I.M.E.* **215,** 577 (1959).

[29] C. W. Price, *Scripta Metall.* **19,** 669 (1985).

[30] C. W. Price, *Scripta Metall.* **23,** 1273 (1989).

[31] E. C. W. Perryman, *Trans. A.I.M.E.* **203,** 1053 (1955).

[32] A. Rosen, M. S. Burton, and G. V. Smith, *Trans. Metall. Soc. A.I.M.E.* **230,** 205 (1964).

[33] P. A. Beck and H. Hu, *Recrystallization, Grain Growth and Textures* (edited by Margolin), p. 393. ASM (1966).

[34] I. L. Dillamore and H. Katoh, *Met. Sci.* **8,** 73 (1974).

[35] A. A. Ridha and W. B. Hutchinson, *Acta metall.* **30,** 1929 (1982).

[36] J. Hjelen, R. Orsund and E. Nes, *Acta metall.* **39,** 1377 (1991).

[37] J. Hirsch and K. Lücke, *Acta metall.* **33,** 1927 (1985).

[38] J. Hirsch and K. Lücke, *Acta metall.* **36,** 2863 (1988).

[39] J. Hirsch and K. Lücke, *Acta metall.* **36,** 2883 (1988).

[40] K. Lücke, *Proc. Seventh Inter. Conf. on the Textures of Mater. (ICOTOM 7)*, (edited by Brakman *et al.*), p. 195. Noordwijkerhout (1984).

[41] A. J. Beaudoin, H. Mecking and U. F. Kocks, *Phil. Mag. A* **73,** 1503 (1996).

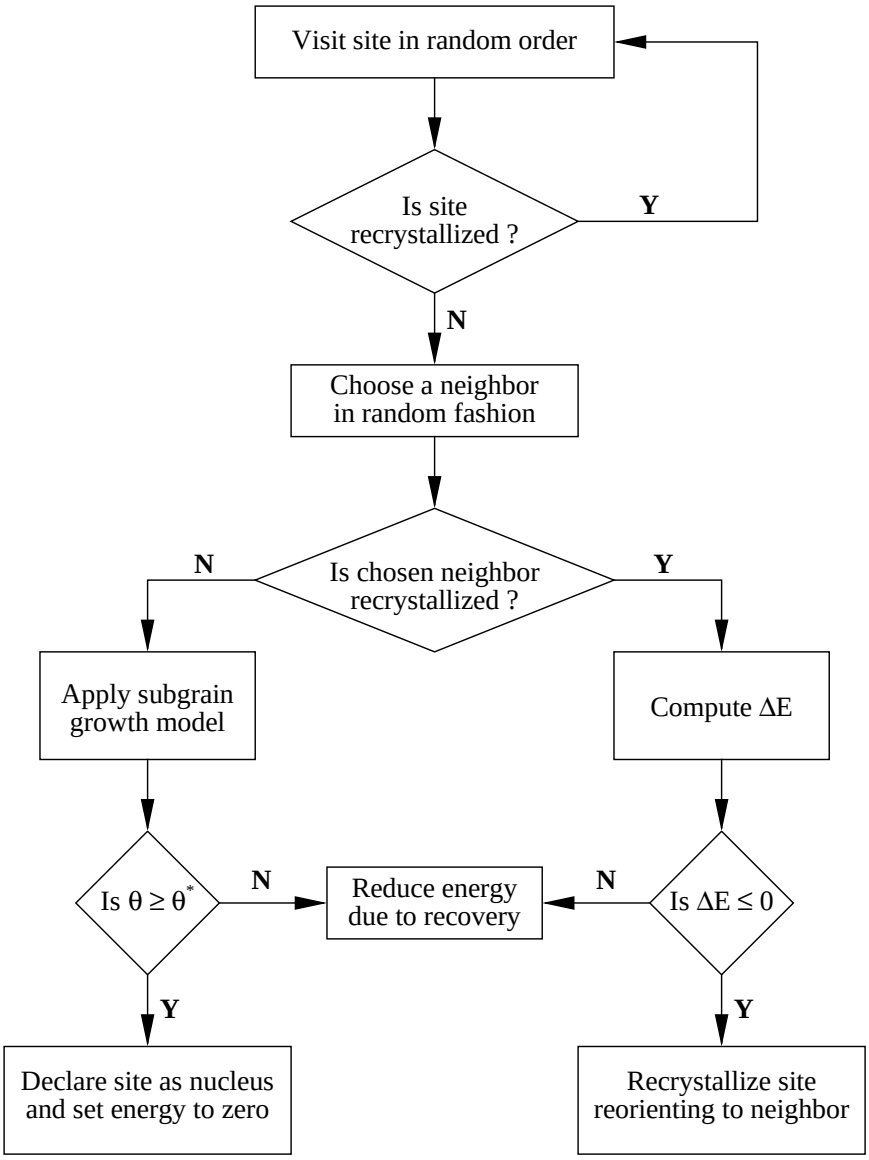

Fig. 1. Flowchart describing the sequence of steps in the simulation at each MCS.

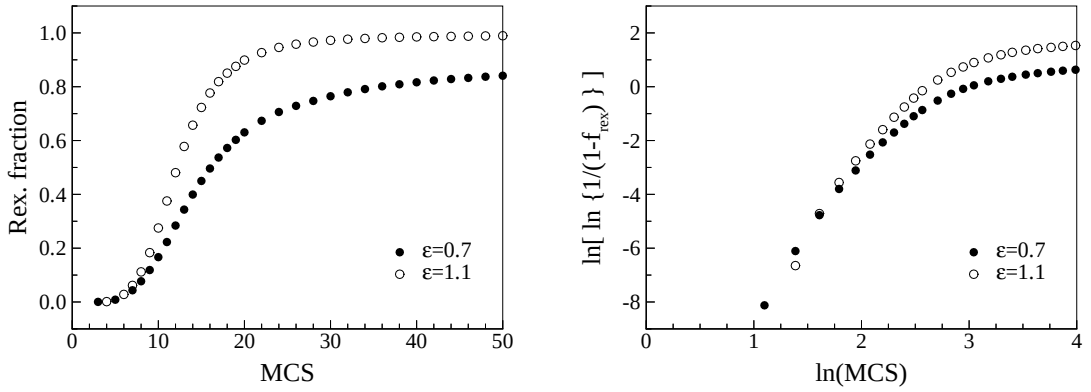

Fig. 2. (a) Variation of recrystallized volume fraction with MCS, (b) Variation of $\ln[\ln\{1/(1-f_{rex})\}]$ with ln(MCS).

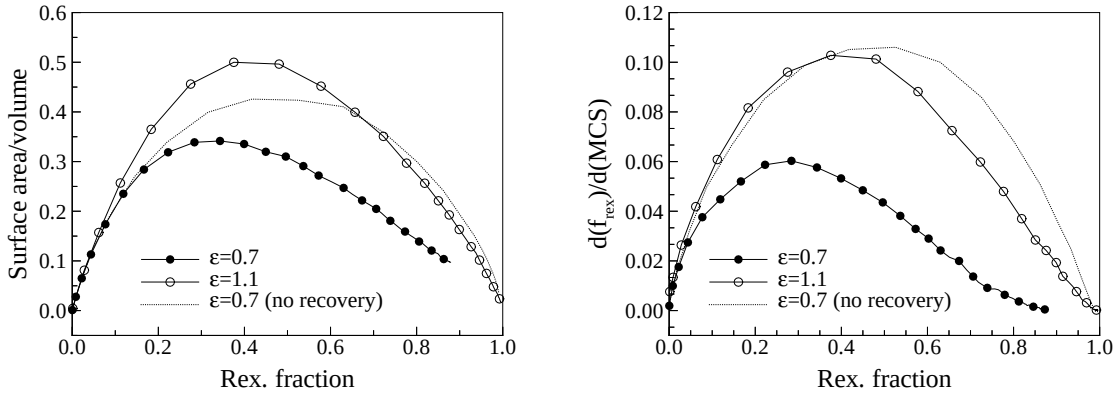

Fig. 3. (a) Evolution of S_v with f_{rex}, (b) Variation of the $d(f_{rex})/d(MCS)$ with MCS.

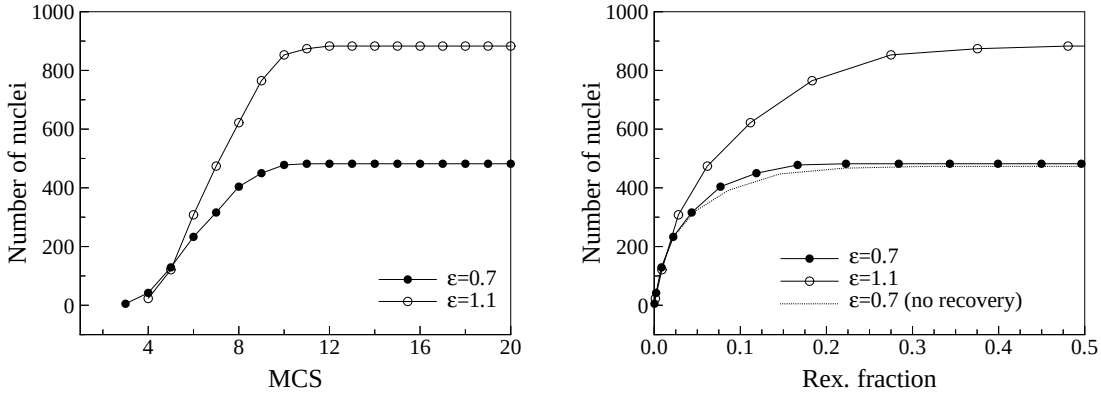

Fig. 4. Variation of total number of nuclei with (a) MCS, and (b) f_{rex}.

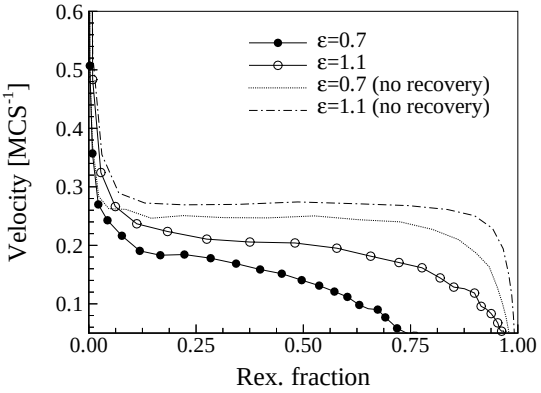

Fig. 5. Mean recrystallization velocity as a function of f_{rex}.

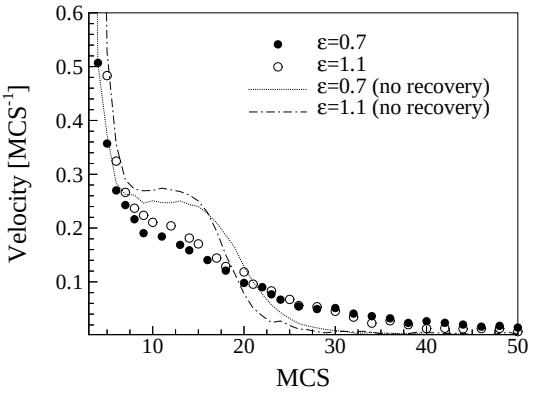

Fig. 6. Mean recrystallization velocity as a function of MCS.

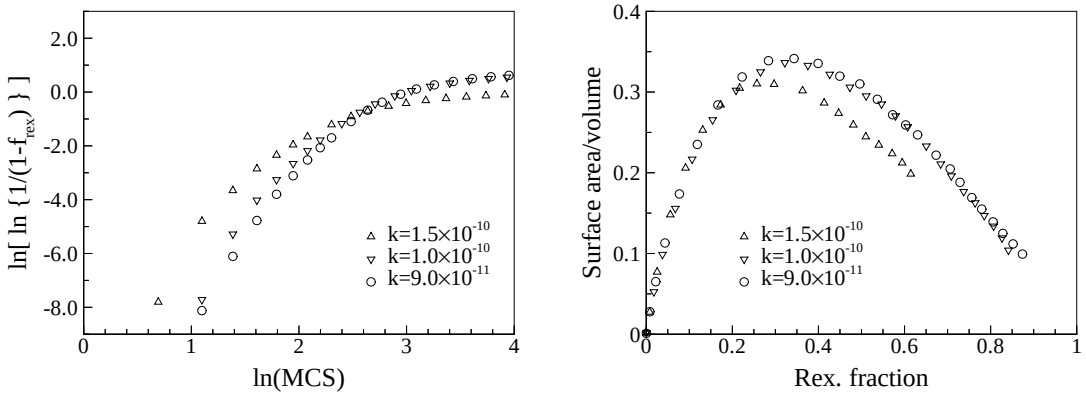

Fig. 7. Variation of (a) recrystallization kinetics, and (b) S_v with the high angle grain boundary mobility for $\varepsilon = 0.7$.

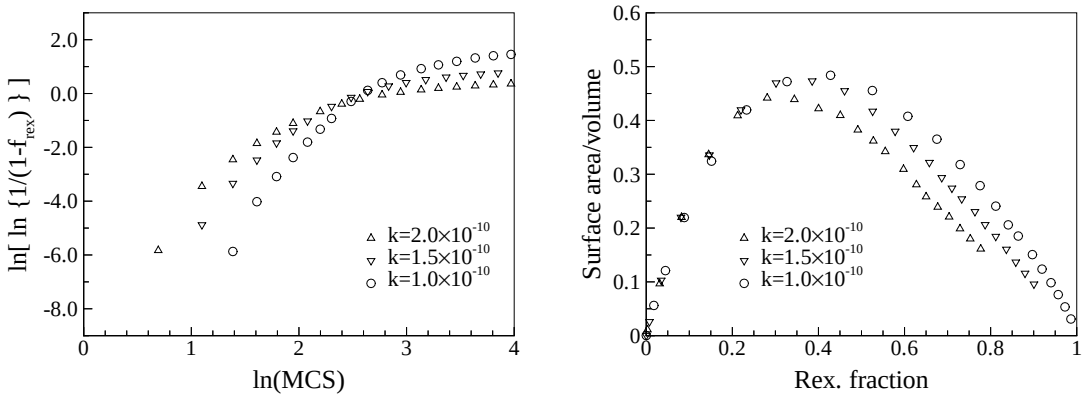

Fig. 8. Variation of (a) recrystallization kinetics, and (b) S_v with the high angle grain boundary mobility for $\varepsilon = 1.1$.

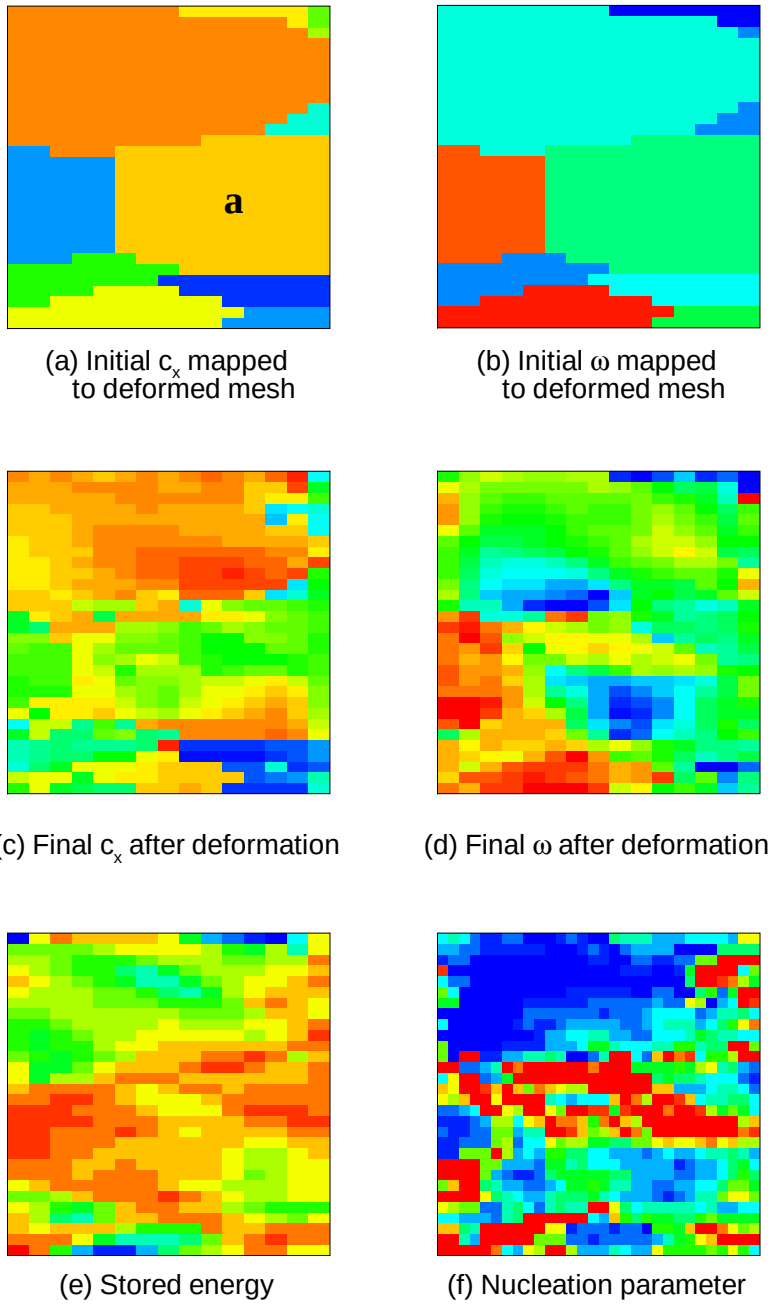

Fig. 9. Grain structure showing (a) initial x-component of axis of rotation, and (b) angle of rotation, mapped to the deformed grid. Grain structures after deformation to $\varepsilon = 0.7$ showing (c) x-component of axis of rotation, (d) angle of rotation, (e) stored energy, and (f) nucleation parameter distributions.

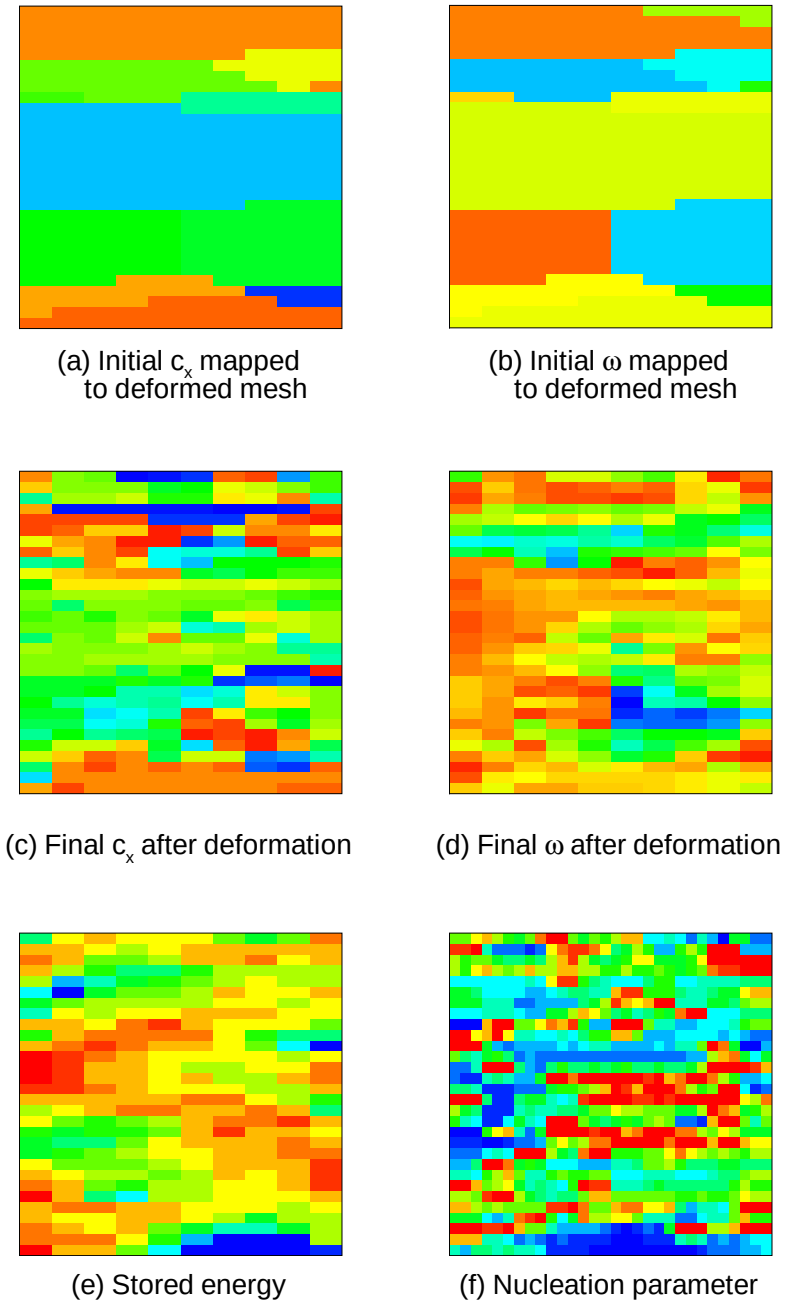

Fig. 10. Grain structure showing (a) initial x-component of axis of rotation, and (b) angle of rotation, mapped to the deformed grid. Grain structures after deformation to $\varepsilon = 1.1$ showing (c) x-component of axis of rotation, (d) angle of rotation, (e) stored energy, and (f) nucleation parameter distributions.

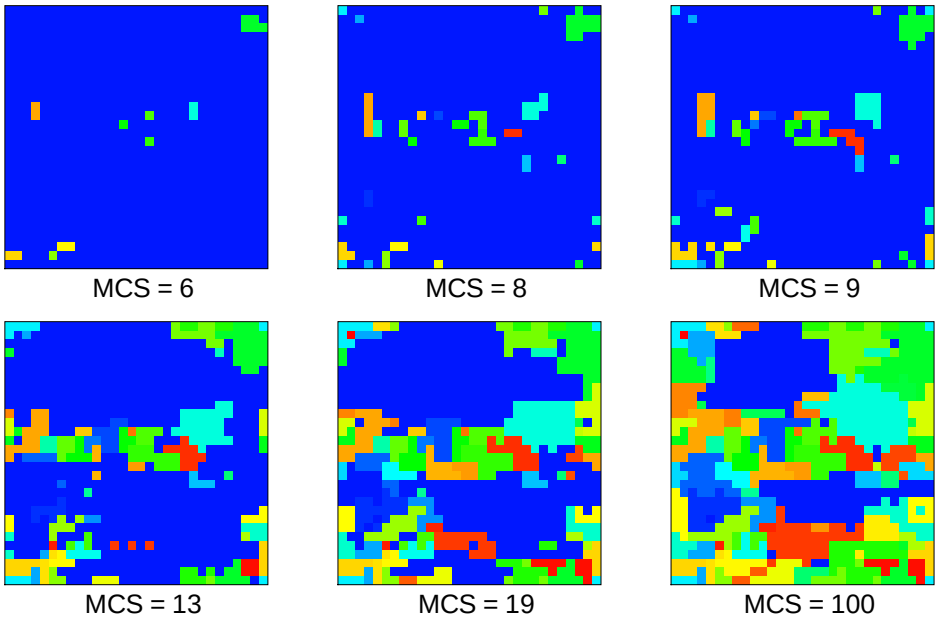

Fig. 11. Temporal evolution of the recrystallized microstructure for $\varepsilon = 0.7$.

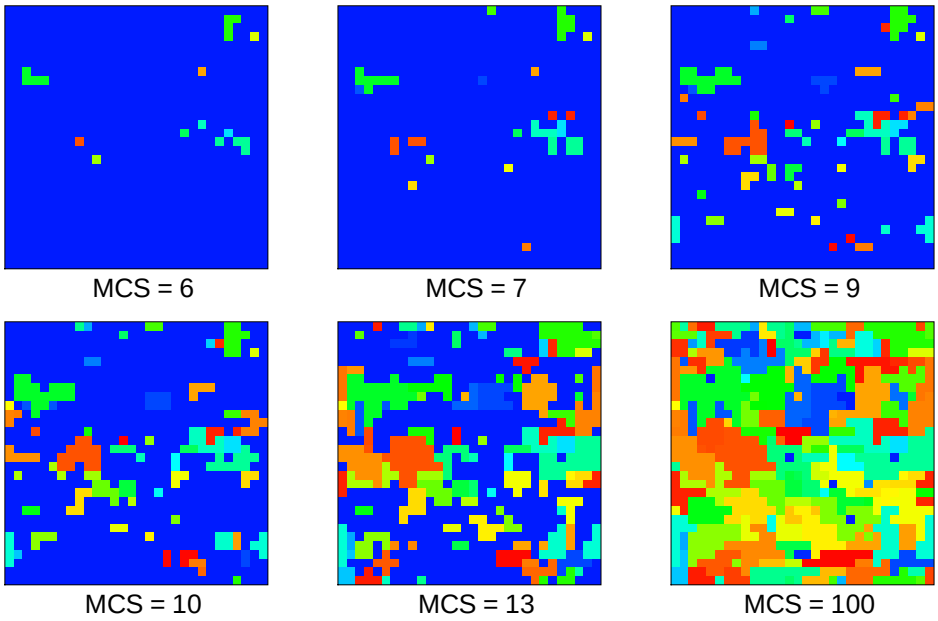

Fig. 12. Temporal evolution of the recrystallized microstructure for $\varepsilon = 1.1$.

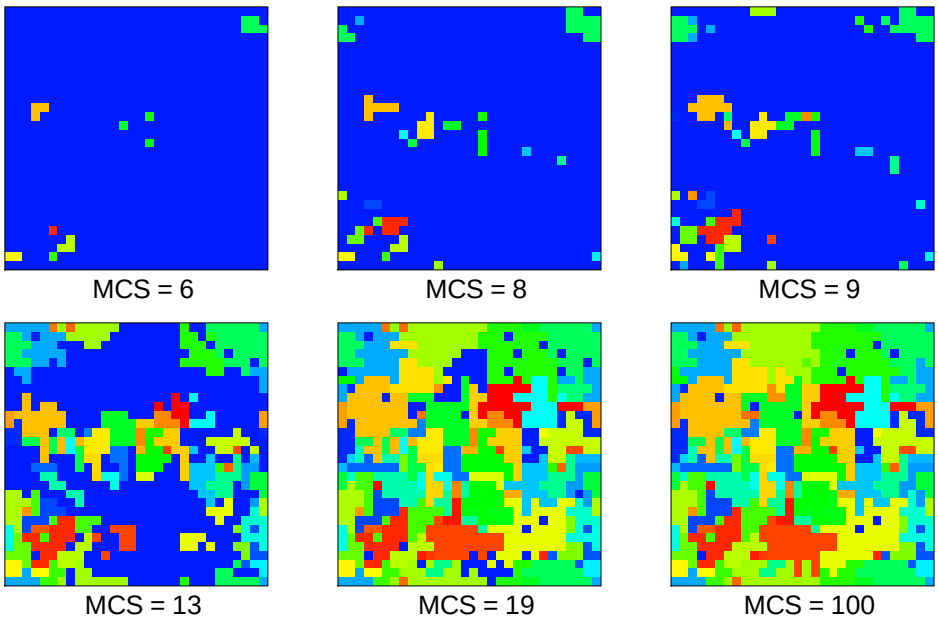

Fig. 13. Temporal evolution of the recrystallized microstructure for $\varepsilon = 0.7$ with no recovery.

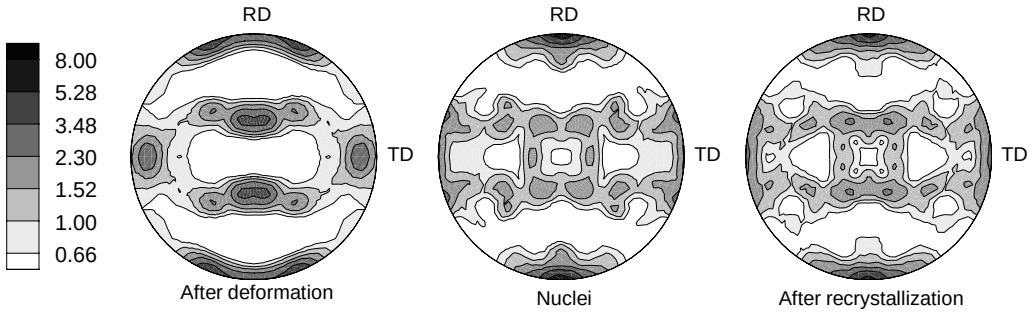

Fig. 14. <111> pole figures in equal area projection showing texture (a) after deformation to $\varepsilon = 0.7$, (b) of recrystallization nuclei, and (c) after growth of nuclei in (b).

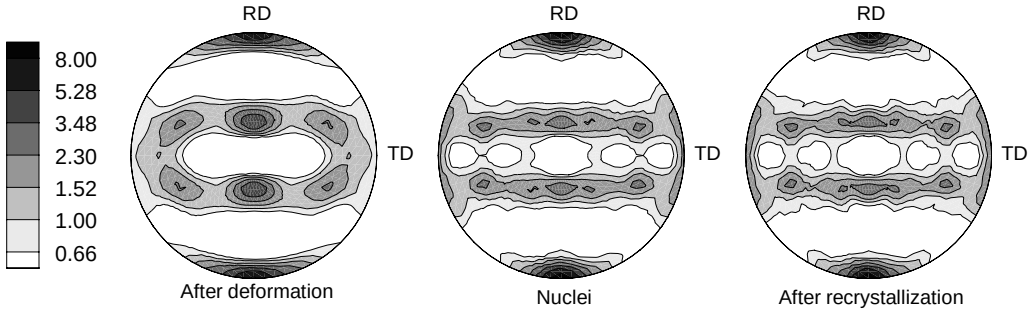

Fig. 15. <111> pole figures in equal area projection showing texture (a) after deformation to $\varepsilon = 1.1$, (b) of recrystallization nuclei, and (c) after growth of nuclei in (b).

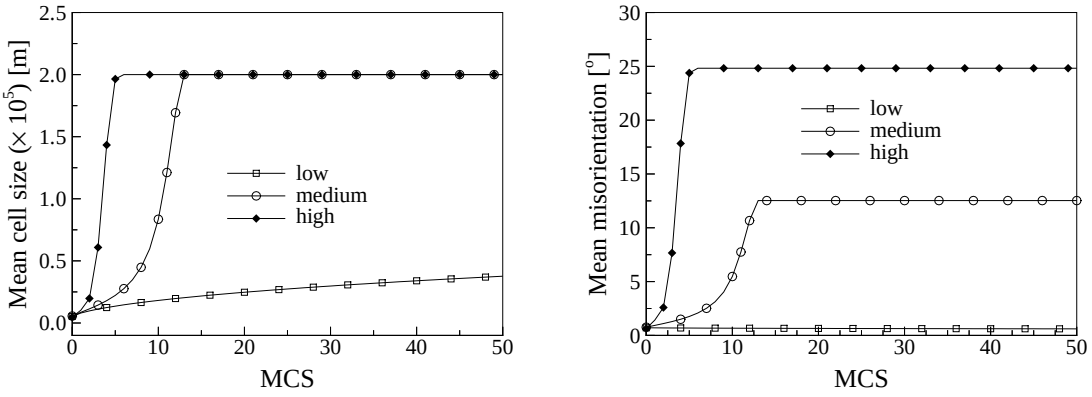

Fig. 16. Variation of (a) mean subgrain size and (b) misorientation with MCS for three different sites with low, medium and high values of the nucleation parameter ν for $\varepsilon = 0.7$.

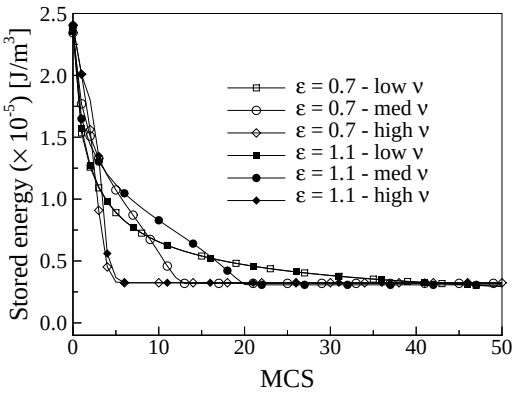

Fig. 17. Variation of stored energy with MCS for three different sites with low, medium and high values of the nucleation parameter ν.